Bounary-Layer Meteorol manuscript No.
(will be inserted by the editor)

Bluff-body flow separation in the lee of a crater rim

Manuela Lehner · C. David Whiteman · Sebastian W. Hoch · Bianca Adler · Norbert Kalthoff

Received: DD Month YEAR / Accepted: DD Month YEAR

Abstract The nearly circular Meteor Crater, Arizona, is located on an extensive, slightly sloping plain, above which a southwesterly katabatic flow forms during undisturbed, clear-sky nights. As the katabatic wind flows over the upstream crater rim, the resulting flow regime in the lee depends on the upstream wind speed. For a shallow katabatic flow with comparatively low wind speeds, the flow decelerates as it approaches the crater. Cold-air intrusions form, that is, cold air spills over the crater rim and runs down the inner southwest sidewall. For a deep katabatic flow with comparatively high wind speeds, the flow accelerates towards the crater. The flow separates in the immediate lee of the crater rim, forming a wake over the southwest crater sidewall. The wake can either be small, affecting only the upper part of the sidewall, or large, affecting the entire crater sidewall or even the crater floor.

When flow separation occurs, the wake region over the crater sidewall is characterized by low wind speeds and potentially a return circulation near the surface. Particularly for large wakes, stability in the crater atmosphere is reduced and relatively high wind speeds can occur at the crater floor, which is otherwise submerged in a strong surface-based inversion. Turbulent kinetic energy at the crater sidewall is typically higher during cold-air intrusions than during flow separation, but high values can occur at the floor when a large wake forms.

Keywords Bluff-body flow separation · Flow over topography · Lee vortex · METCRAX II · Wake

M. Lehner
Department of Atmospheric and Cryospheric Sciences, University of Innsbruck, Innrain 52f, 6020 Innsbruck, Austria
E-mail: manuela.lehner@uibk.ac.at

C. D. Whiteman and S. W. Hoch
Department of Atmospheric Sciences, University of Utah, Salt Lake City, Utah, USA

B. Adler and N. Kalthoff
Karlsruhe Institute of Technology, Karlsruhe, Germany

1 Introduction

As air flow interacts with topography, that is, as air is either forced to flow over mountains or depressions or to flow around them, the resulting flow regimes and processes depend strongly on flow characteristics (i.e., stability and speed) and on topographic characteristics (e.g., mountain height and width, lateral extension, slope angle, and surface roughness) (e.g., Vosper 2004; Jackson et al. 2012; Lehner et al. 2016a; Rotunno and Lehner 2016). As air flows around obstacles, vertical-axis vortices can form in the lee (e.g. Smolarkiewicz and Rotunno 1989; Katurji et al. 2013). The resulting wake region in the lee is typically characterized by reduced mean wind speeds and high turbulence (Katurji et al. 2013). Lee vortices with a horizontal axis, on the other hand, can form as air flows over obstacles and separates from the surface in the lee, resulting, for example, in turbulent rotors (e.g. Doyle and Durran 2007) or recirculation zones in the immediate lee of the mountain (e.g., Gerber et al. 2017; Menke et al. 2018).

Boundary-layer or flow separation in the lee of obstacles can occur due to the presence of an adverse pressure gradient that causes a deceleration of the flow, particularly in the near-surface layer (e.g., Wood 1995; Belcher and Hunt 1998; Ambaum and Marshall 2005). Baines (1995) defines three different boundary-layer-separation regimes based on laboratory experiments: (i) boundary-layer separation at the mountain crest (i.e., bluff-body flow separation), (ii) flow separation farther down the lee sidewall below the first wave crest, which he calls post-wave separation, and (iii) complete attachment, that is, no separation occurs. The three flow types are characterized by their location in a regime diagram as a function of H/W and NH/U, where H is the mountain height, W is the length of the lee slope, N is the buoyancy frequency, and U is the upstream wind speed. The formation of bluff-body flow separation depends on the ratio between the wavelength of the internal waves $2\pi U/N$ and W so that boundary-layer separation can occur if $NW/U < \pi$. Post-wave separation, on the other hand, can occur when NH/U is above a critical threshold value.

Ambaum and Marshall (2005) derived a vorticity equation to describe accelerations and decelerations for flow over a hill. They assumed that flow-separation will occur if the decrease in flow speed is large enough, that is, of the same order of magnitude as the unperturbed base-state velocity. For small aspect ratios (i.e., small hills) linear solutions to their equation reproduced the regime diagram by Baines (1995). According to their solutions, the location of flow deceleration and thus flow-separation depends on the flow solution, that is, whether the solution is evanescent or wave-like. For evanescent solutions, deceleration occurs along the lee slope of the hill and flow separation in the immediate lee of the hill is thus possible if flow deceleration is large enough. For wave-like solutions, deceleration starts farther downstream over the lee slope of the hill. If flow separation occurs, it will thus be in the form of post-wave separation.

Post-wave separation is closely related to rotor formation in the lee of mountains. Rotors form when the boundary layer separates from the surface because of adverse horizontal pressure gradients that occur in connection with trapped lee waves (Doyle and Durran 2002, 2007; Vosper 2004). Vertical wind shear close to the surface produces a thin layer of positive vorticity, which is lifted into the wave. Hertenstein and Kuettner (2005) identified a second type of rotor based on numerical simulations, which is reminiscent of a hydraulic jump and which results from negative vorticity being produced by the baroclinicity in connection with the deformation of an inversion layer. The two types of rotors were also observed experimentally in the lee of the Medicine Bow Mountains, Wyoming, by French et al. (2015).

Idealized simulations with a two-layer atmosphere by Vosper (2004) showed that if the Froude number $F = U/\sqrt{g' z_i}$ is within a certain range that allows the formation of trapped lee waves and if $H/z_i \geq 0.3$ the wave amplitude becomes large enough to cause rotor formation, where z_i is the depth of the lower layer and $g' = g\Delta\theta/\theta_0$ is the reduced acceleration of gravity, with g the acceleration of gravity, $\Delta\theta$ the potential temperature difference across the inversion separating the lower from the upper layer and θ_0 the reference potential temperature in the lower layer. Doyle and Durran (2002) defined a non-dimensional pressure gradient threshold criterion for post-wave flow separation based on idealized simulations. Applying this criterion to observations in the lee of the Medicine Bow Mountains, Wyoming, Strauss et al. (2016) found, however, that flow separation can occur for even smaller pressure gradients. They suggest that in addition to pressure-gradient forces, buoyancy forces may contribute to flow deceleration and thus boundary-layer separation.

Bluff-body flow separation in the lee of obstacles has been shown in water tank studies (e.g., Baines and Hoinka 1985) and occasional observations in the atmosphere have been reported, for example, in the lee of the Sierra Nevada by Grubišić and Doyle (2006). Lidar observations by Gerber et al. (2017) showed recirculation in the lee of the Sattelhorn Ridge in the Dischma Valley, Switzerland, which persisted for more than 16 h with a horizontal extent of 400–1000 m and a vertical extent of up to about 200 m. Indirect observations of flow separation have also been reported. Strauss et al. (2015) observed high turbulence values in the immediate lee of the Medicine Bow Mountains suggesting the presence of bluff-body flow separation. A visualization of horizontal-axis lee vortices occurs when clouds form. Vortices in the immediate lee of mountain peaks have been identified as the most likely formation mechanism for so-called banner clouds (Wirth et al. 2012; Voigt and Wirth 2013).

As indicated by Baines (1995), the occurrence of bluff-body flow separation in the lee of an obstacle depends on the speed of the approaching flow and on the stability. Mason (1987) observed flow separation or decoupling in a small, approximately 200-m deep valley under neutral and unstable conditions, while the flow remained attached under stable conditions with a Froude number smaller than 2, and was able to reproduce that result with numerical simulations. Similar results were found by Holden et al. (2000) based on tethersonde measurements, who also related the decoupling of the flow to the Richardson number, with decoupling occurring at relatively high Richardson numbers. Idealized simulations of flow over small basins by Lehner et al. (2016a) produced flow separation over the upstream basin edge in their highest-wind speed simulations (15 m s^{-1}) with the deepest basins (100 and 150 m). Menke et al. (2018) probed a recirculation zone in the lee of two parallel mountain ridges in central Portugal at three different cross sections with six scanning Doppler lidars and found that reversed flow greater than 0.5 m s^{-1} occured 50% of the time and that the occurrence of the recirculation zone depended on stability (specifically, most frequent occurrence for near-neutral and unstable conditions), on wind speed (most frequent occurrence for wind speeds larger than 8 m s^{-1}), and on the topography, that is, they observed variations among the three different cross sections.

Flow separation also strongly depends on the topography, for example, the sharpness of the mountain top, with separation being more likely in the presence of salient edges (Batchelor 1967; Kim et al. 2001). Flow separation and the formation of a recirculation zone in the lee is also facilitated by steeper slopes (Arya et al. 1987; Kim et al. 2001; Wood 1995) and by denser canopies, that is, higher surface roughness (Wood 1995; Poggi and Katul 2007; Patton and Katul 2009). Wood (1995), for example, estimated the critical slope angle for flow separation based on idealized simulations, finding a lower critical slope angle for higher surface roughness. They also showed that for 2D cases, the separation point moves upstream with increasing hill height and that the recirculation eddy size increases.

In this paper we present nighttime observations of bluff-body flow separation at the rim of Arizona's Meteor Crater during comparatively high-wind-speed periods. The wake that forms over the southwest crater sidewall is characterized by low wind speeds and sometimes a return flow near the surface, that is, an upslope flow component. Section 2 describes the Meteor Crater and the dataset used in this study. Evidence for flow separation in the lee of the crater rim is presented in Sect. 3. The atmospheric conditions leading to flow separation and the characteristics of the flow in the resulting wake region are described in Sect. 4 and Sect. 5, respectively. Finally, a brief summary and conclusions are given in Sect. 6.

2 Data and Methods

2.1 The Meteor Crater

The Meteor Crater in northern Arizona (35°N, 111°W) is a nearly circular, bowl-shaped basin that was produced by a meteorite impact 49000 yr ago (Fig. 1). It is about 1.2 km in diameter, 170 m in depth, and is surrounded by a rim that extends 30–50 m above the surrounding plain, which rises slightly to the southwest with a slope angle of about 1°. Two major field campaigns, METCRAX (Meteor Crater Experiment; Whiteman et al. 2008)

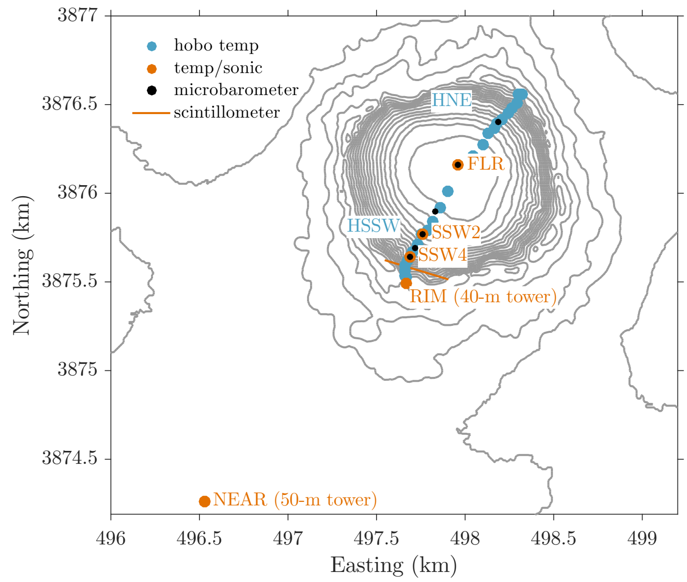

Fig. 1 Topography of the Meteor Crater with the location of the measurement sites used in this study. Elevation contour lines are at 10-m intervals.

and METCRAX II (Lehner et al. 2016b), took place at the Meteor Crater to study various aspects of the crater meteorology. The focus of METCRAX II in October 2013 was on the flow past the crater basin. During clear-sky, quiescent nights a surface-based inversion and a southwesterly katabatic flow form over the plain surrounding the Meteor Crater, with a typical inversion depth and strength of about 50 m and 0.15 K m^{-1}, respectively, and a jet maximum of 5 m s^{-1} at 30 m above ground level (AGL; Whiteman et al. 2018a). Once the depth of the inversion exceeds the height of the crater rim, the cold air starts to drain into the crater over the upwind, southwest rim until the air reaches its level of neutral buoyancy (Whiteman et al. 2018a). This inflow of cold air modifies the nocturnal stratification within the crater, resulting in a shallow and strong surface-based inversion above the crater floor, which is topped by a deep near-isothermal layer and a capping inversion near the top of the crater (Whiteman et al. 2010; Haiden et al. 2011). With a deepening of the katabatic flow upstream and an increase in wind speed, the flow over the crater topography can also lead to the formation of a wave over the basin, which can reach amplitudes exceeding the crater depth (Adler et al. 2012; Whiteman et al. 2018b).

2.2 Data

The data used in this study come from the METCRAX II experiment. A detailed description of the METCRAX II field campaign, the measurement sites, and the instrumentation can be found in Lehner et al. (2016b). The measurement sites used in this study are shown in Fig. 1. The data come from two lines of hobo temperature data-loggers (Onset Computer, Inc., Bourne, Massachusetts), which ran up the northeast and south-southwest crater sidewalls (labeled HNE and HSSW in Fig. 1), with eleven and twelve sensors, respectively. Instantaneous temperature values were recorded every 2.5 min. A 40-m high tower was installed at the crater rim (RIM), which was instrumented with CSAT3 sonic anemometers and hygrothermometers at 5 m intervals. A similarly instrumented 50-m high tower was installed about 1.6 km upstream, that is, southwest, of the Meteor Crater (NEAR), with the lowest measurement level at 3 m instead of 5 m to be used as part of a full energy-balance station. Additional sonic anemometers were installed at two sites along the south-southwest crater sidewall, 40 (SSW2) and 90 m (SSW4) above the crater floor, and at the crater floor itself (FLR). Wind data from the sonic anemometers were tilt corrected (Wilczak et al. 2001) and turbulence statistics were calculated for 5-min averaging intervals from the 20-Hz measurements. Further data come from a network of microbarometers in the crater, specifically at FLR, SSW2, SSW4, a site located in-between SSW2 and SSW4 (SSW3, 70 m above the crater floor), and a site downslope from SSW2 (SSW1, 10 m above the crater floor). Pressure was sampled with a frequency of 1 Hz and averaged over 5-min intervals for the analysis. Pressure measurements from the southwest sidewall are analyzed with respect to data from a microbarometer on the relatively undisturbed northeast sidewall (NNE, 50 m above the crater floor). Sites SSW1, SSW3, and NNE are not labeled in Fig. 1. Turbulence measurements in the immediate lee of the southwest crater rim were made with a surface layer scintillometer (SLS20, Scintec).

Data are analyzed for the period 4–29 October, when all of these instruments were operational. The analysis is restricted to nighttime periods between 1800 and 0600 MST and to periods when (i) an inversion was observed at NEAR between the top and the bottom levels of the tower ($T_{50m} - T_{3m} > 0$) and (ii) the wind direction at 50 m AGL at NEAR was from a southwesterly direction (165–255°) to indicate a katabatic flow. These criteria had to be met for at least one continuous hour based on 5-min averaged data values for the data to be included in the analysis.

3 Flow Separation in the Meteor Crater

An analysis of the cold-air intrusions coming over the southwest crater rim during Intensive Observational Period (IOP) 7 (26–27 October) showed temporal increases in wind speed along the southwest sidewall in connection with changes in the level of neutral buoyancy of the cold air coming over the crater rim (Whiteman et al. 2018a). Specifically, SSW2 in the lower part of the sidewall (see Fig. 1) is located close to the top of the shallow (30–40 m) and strong (5–10 K potential temperature change) surface-based inversion, with low wind speeds close to 0 m s^{-1} when unaffected by the intrusions. When the level of

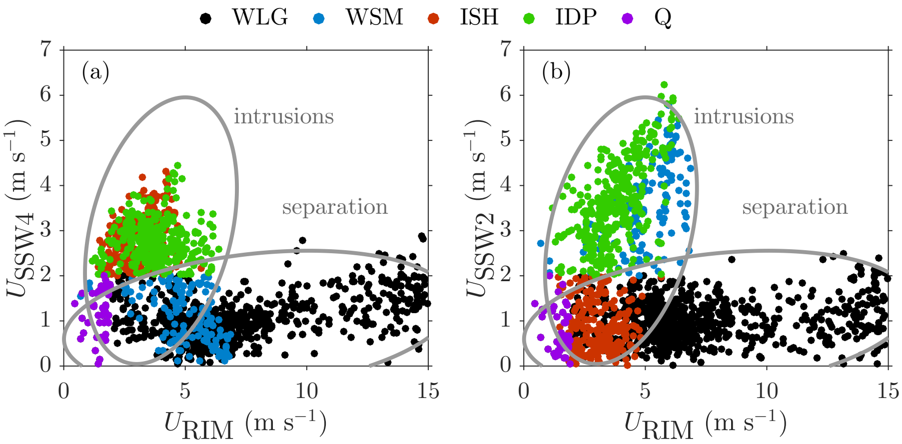

Fig. 2 Wind speed at (a) SSW4 and (b) SSW2 as a function of the mean wind speed at RIM. See text for a description of the five different colour-coded categories.

neutral buoyancy of the cold air running down the crater sidewall descends below SSW2, an increase in wind speed to about 3–5 m s^{-1} is observed.

Plotting the wind speed along the southwest sidewall at SSW4 and SSW2 against the wind speed averaged over the 40-m deep layer sampled at the crater rim for the entire month, however, reveals the presence of two different flow regimes (Fig. 2). In the first or *intrusion regime* with relatively low wind speeds at RIM of less than about 5 m s^{-1}, wind speeds along the sidewall have a similar magnitude as the wind speed at the rim. SSW2 also shows a close-to-linear increase in wind speed with increasing speed at RIM. In the second or *separation regime* with higher wind speeds at RIM of about 5 m s^{-1} or more, weak wind speeds, generally less than 2 m s^{-1} are observed along the sidewall and increasing the wind speed at the RIM to 10 m s^{-1} and more does not lead to further increases in wind speed along the sidewall. This suggests the formation of a wake over the sidewall as a result of flow separation in the lee of the crater rim. For wind speeds greater than about 7 m s^{-1} at the rim, only the flow-separation regime seems to occur. For wind speeds lower than about 7 m s^{-1}, however, either low or high wind speeds can be observed along the sidewall. For very low wind speeds it is of course difficult to distinguish between the two regimes based on the wind speed along the southwest sidewall, because even for the intrusion regime only low wind speeds would be expected to occur. Results similar to Fig. 2 are obtained if the mean wind speed at RIM is replaced with the maximum wind speed over the eight vertical levels, or with the values at the bottom and top of the 40-m tower. The five categories indicated by different colours in Fig. 2 and in the background of Fig. 3 will be discussed in Sect. 4.

Figures 3a–c show an example of a cold-air-intrusion dominated night (26–27 October; IOP 7), the same night that was analyzed by Whiteman et al. (2018a). Wind speeds at SSW4 are of a similar magnitude as wind speeds at

5 m AGL at RIM and the wind direction is from the southwest, indicating a flow down the slope (Figs. 3a, b). Wind speeds, and to a lesser degree wind directions, are more variable at SSW2, showing strong increases and decreases in wind speed, which indicate whether the cold-air intrusion penetrates below SSW2 or whether it reaches its level of neutral buoyancy already above SSW2 (Whiteman et al. 2018a). A strong inversion is present in the lowest layer of the crater atmosphere, with the potential temperature near the crater floor 5–10°C lower than at the crater rim and in the upper part of the northeast sidewall (Fig. 3c). Whiteman et al. (2018a) have shown that the temperature measurements along the northeast sidewall are representative of the vertical temperature structure in the quiescent nocturnal crater atmosphere when disturbances are restricted to a shallow cold-air intrusion layer over the southwest sidewall. Wind speeds at the crater floor at the bottom of the inversion are weak and wind direction is correspondingly variable.

During the night of 16–17 October (IOP 3; Figs. 3d–f), flow separation occurred over the southwest sidewall. Wind speeds at SSW4 are comparatively low, typically below 2 m s^{-1}, and generally decrease at the same time as wind speeds increase at RIM and vice-versa (Fig. 3d). For example, around 0030 MST, the wind speed increases at RIM and simultaneously decreases at SSW4. Around 0200 MST, the opposite occurs and the two wind speeds become almost identical for a short period of time, before the wind speed increases again at RIM and drops to almost 0 m s^{-1} at SSW4. This regime then lasts for almost two hours until about 0400 MST. The wind direction during this period of near-calm conditions turns mostly to a northeasterly upslope direction, indicating a return circulation within the wake region (Fig. 3e). A return circulation, however, does not form during all other flow-separation periods, which could be related to the fact that there is constant forcing for a thermally driven downslope flow opposing the return circulation. In contrast to SSW4, wind speeds at SSW2 are generally high during this night, with winds from a southwesterly, downslope direction, suggesting that the flow reattaches to the surface downstream of the wake. Near-calm winds at FLR are again consistent with a decoupling of the lowest basin atmosphere, although the stability is generally weaker during this night than during the intrusion-dominated night of the 26–27 October (Fig. 3f). Particularly during the two flow-separation periods around 0100 MST and between 0200 and 0400 MST, the potential temperature near the crater floor is only slightly lower than in the upper part of the crater, indicating an almost mixed crater atmosphere. During the short break around 0200 MST and after 0400 MST, the temperature in the lower part of the crater drops, leading to the formation of a new crater-floor inversion.

While the wake during the night of 16–17 October extends only to SSW4 but not to SSW2, where relatively high wind speeds are observed, larger wakes can also form that extend farther down the southwest sidewall. An example is shown in Figs. 3g–i for the night of 27–28 October. Wind speeds along the southwest sidewall are generally weak, both at SSW4 and SSW2, while wind speeds at RIM exceed 5 m s^{-1} (Fig. 3g). Wind speeds at FLR are also higher

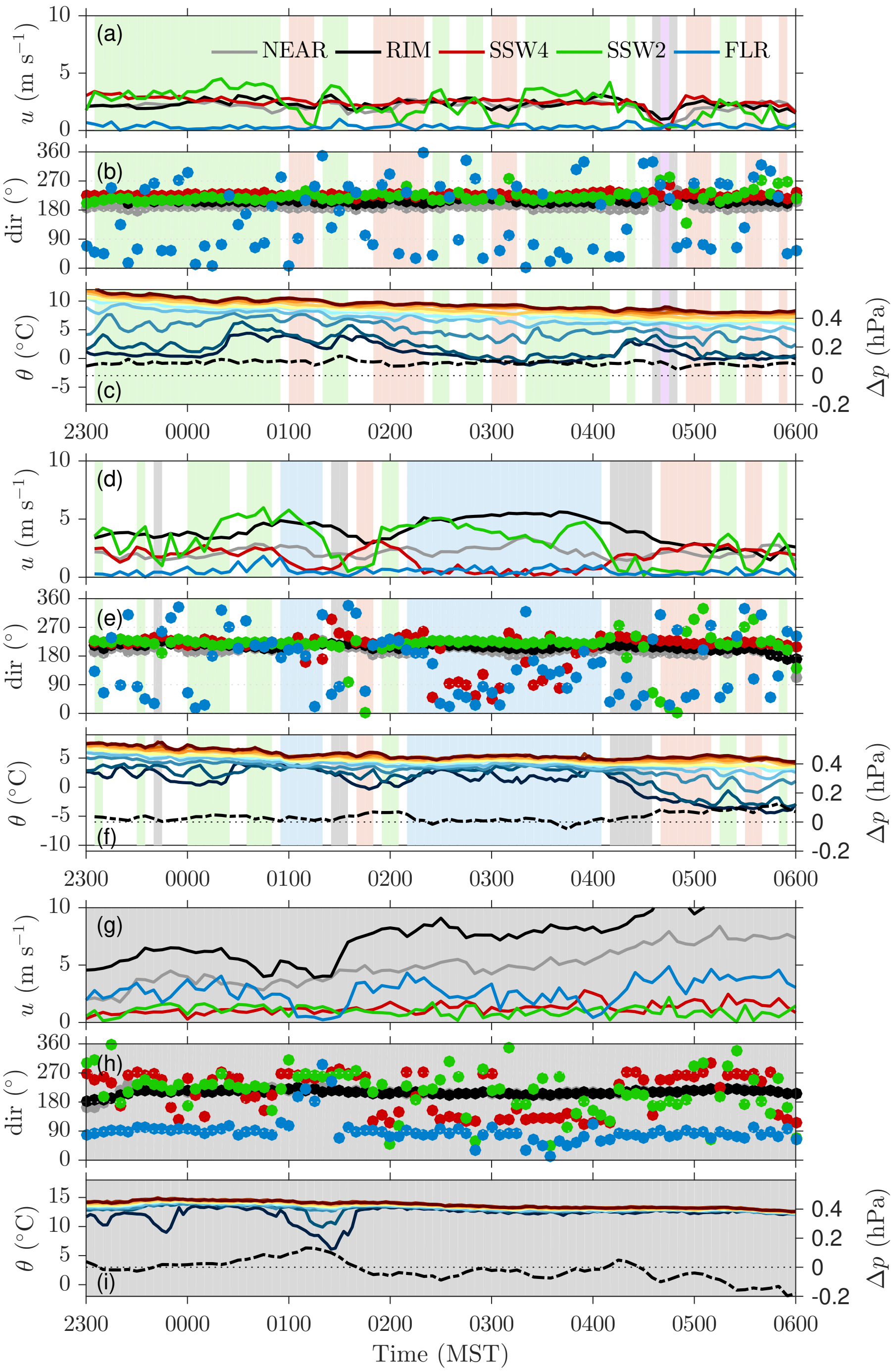

Fig. 3 Time series of (a,d,g) wind speed and (b,e,h) wind direction at NEAR (3 m AGL), RIM (5 m AGL), SSW4, SSW2, and FLR; (c,f,i) potential temperature (left axes) at different sites running up the northeast sidewall from the crater floor (dark blue) to the rim (dark red) at approximately 10–20 m height intervals and pressure difference between RIM and NEAR (right axes; dashed line) on (a–c) 26–27, (d–f) 16–17, and (g–i) 27–28 October. The colour-coded background is explained in Sect. 4.

than over the sidewall and the wind direction is consistently from the northeast (Fig. 3h), that is, opposing the southwesterly flow over the crater, suggesting the formation of a large crater-sized eddy. This is consistent with a well-mixed crater atmosphere, with a brief exception between 0100 and 0200 MST, when a shallow, about 5 m deep layer cools above the crater floor (Fig. 3i). This short period coincides with slightly reduced wind speed at RIM and near-calm conditions at FLR (Fig. 3g).

4 Conditions for Flow Separation

Figure 2 showed that the wind speed within the wake region is generally less than about 2 m s^{-1}. We can thus use this information to identify wake occurrences objectively for further analysis. Because Fig. 2 also shows individual wake events with slightly higher wind speeds than 2 m s^{-1} when the wind speed at the rim is very high, times with wind speeds exceeding 7 m s^{-1} at the rim are also classified as wakes independent of the wind speed at SSW2 and SSW4. Based on this classification scheme and on the information provided by the examples in Fig. 3, we define five different categories: (i) A large wake or complete decoupling of the crater atmosphere similar to the night of 27–28 October (Figs. 3g–i) is defined when the wind speed at RIM is larger than 7 m s^{-1} or when the wind speeds at both SSW2 and SSW4 are below 2 m s^{-1} (WLG—large wake). (ii) A small wake that affects only the upper part of the southwest sidewall similar to the night of 16–17 October (Figs. 3d–f) is defined when the wind speed at rim is less than 7 m s^{-1} and the wind speed at SSW4 is below 2 m s^{-1}, but the wind speed farther down the slope at SSW2 is larger than 2 m s^{-1} (WSM—small wake). (iii) A cold-air intrusion that does not extend to SSW2 similar to the period shortly after 0300 MST during the night of 26–27 October (Figs. 3a–c) is defined when the wind speed is higher than 2 m s^{-1} at SSW4 but lower than 2 m s^{-1} at SSW2 (ISH—shallow intrusion). (iv) A cold-air intrusion that reaches beyond SSW4 similar to, for example, the period after about 0315 MST during the night of 26–27 October (Figs. 3a–c) is defined when the wind speeds at both SSW2 and SSW4 exceed 2 m s^{-1} (IDP–deep intrusion). (v) Finally, a quiescent category is defined for those cases when the wind speeds at RIM and at both SSW4 and SSW2 are less than 2 m s^{-1} (Q—quiescent), which are not likely to be wake cases in spite of the low wind speeds over the southwest sidewall. These five regimes are color-coded throughout the remainder of this paper and added as background colours in the time series of the three case studies, similar to Figs. 2 and 3. The background colors in Fig. 3 thus indicate, for example, an approximately 2-h long small wake around 0300 MST on 16–17 October (Figs. 3d–f) and the presence of a large wake during the entire night of 27–28 October (Figs. 3g–i).

The criterion for lee-side flow separation defined by Baines (1995) states that the half-length of the obstacle in the lee has to be smaller than the half wavelength of the internal waves excited by the obstacle, that is, $NA_d/U < \pi$, where A_d is the half-width of the obstacle. Using an approximate half-width

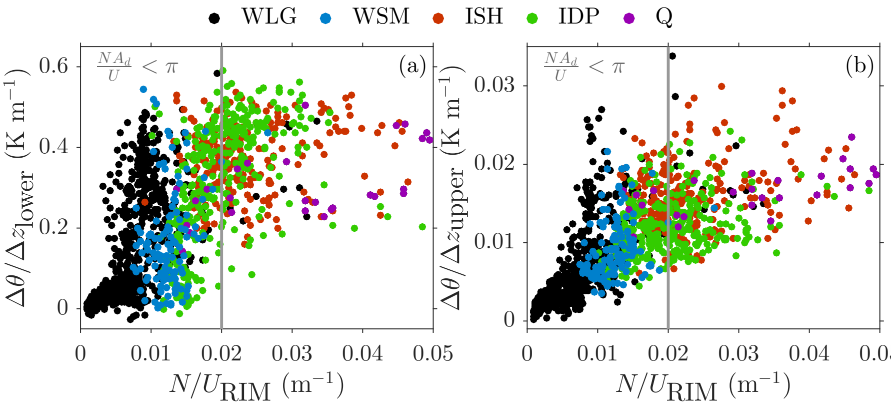

Fig. 4 Pseudo-vertical potential temperature gradients across (a) the lower 25 m and (b) the top 91 m as a function of N/U at RIM. Potential temperature gradients were calculated from temperature sensors on the northeast sidewall and N and U were averaged over the 40-m tower. The criterion for flow separation by Baines (1995) is indicated by a vertical grey line. Note the different ranges of the potential temperature gradient in two figures.

of 150 m for the Meteor Crater, the resulting N/U is $\pi/150 \approx 0.02$ m^{-1}. Figure 4 shows scatter plots of the stability in the crater, that is, the vertical potential temperature difference across fixed layers, as a function of N/U at RIM, where N and U have been averaged over the 40-m high tower. Potential temperature gradients in the crater are pseudo-vertical gradients, that is, they were calculated from the near-surface temperature measurements along the northeast sidewall. The data show a regime transition around 0.015 m^{-1}, with flow separation occurring for N/U <0.015 m $^{-1}$, that is, slightly below the criterion defined by Baines (1995). It has to be kept in mind, however, that N and u vary with height and that the mean values are thus only approximations, as is the estimate of A_d. Small wakes, which affect only SSW4, occur at the upper end of this range between about 0.007 and 0.015 m^{-1}.

The criterion by Baines (1995) contains the stability upstream or at the crater rim. Strauss et al. (2016), however, suggested that the stability in the valley downstream may also facilitate or prevent flow separation. Although their argument was made for post-wave separation and rotor formation, it is also considered here for bluff-body separation. The nocturnal atmosphere in the Meteor Crater is typically characterized by a strong and shallow inversion at the crater floor, with a close to isothermal layer above (Whiteman et al. 2010, 2018b). The pseudo-vertical potential temperature gradients across the lowest 25-m deep layer, that is, within the crater-floor inversion, and across the top 91-m deep layer, that is, within the near-isothermal layer are shown in Fig. 4. The potential temperature gradients were calculated from four hobo temperature sensors on the northeast sidewall, which best represents ambient conditions within the crater. As already seen for the three case studies presented in Fig. 3, the stability in the lower part of the crater is much higher during intrusions than during flow separation. Particularly for large wakes, the crater atmosphere is close to neutral throughout its entire depth. This is likely a result of increased wind speeds and thus mixing in the crater during this flow regime. Small wakes, which only affect the upper part of the southwest crater sidewall, are, however, not likely to lead to a mixing of the entire crater themselves. Figure 4b shows that their occurrence is usually also accompanied by lower stabilities compared to intrusions, also in the upper, near-isothermal layer, which may thus facilitate flow separation.

Stiperski et al. (2018) analyze vertical profiles upwind of the crater at NEAR and distinguish two different types of katabatic flows approaching the crater. A shallow type with a jet maximum at 15–25 m AGL and a deeper type with the jet maximum near the top of the 50-m tower. The latter is also characterized by weaker directional wind shear with height and weaker near-surface stratification. These differences in the katabatic flow profiles can have different effects on the crater atmosphere. While nearly continuous cold-air intrusions over the southwest rim into the crater basin occur during shallow katabatic-flow periods (Whiteman et al. 2018a), large-amplitude waves can form over the basin with increased flow speeds along the southwest sidewall during deep katabatic flows (Adler et al. 2012; Whiteman et al. 2018b). Figure 5 shows wind and stability profiles at NEAR and RIM for the five different flow categories. Both intrusion categories and also the quiescent conditions are characterized by a distinct jet profile. The wind profiles show a jet maximum of about 5 m s^{-1} around 25 m AGL at NEAR and a stability maximum at about 15 m AGL for both intrusion regimes. This agrees with the finding by Whiteman et al. (2018a) that flow intrusions occur with a shallow katabatic flow. The wind and stability profiles for the wake cases agree better with the deep katabatic flow described by Stiperski et al. (2018), with a continuous increase in wind speed throughout the height of the 50-m tower and comparatively lower stability. For the large wakes, the 90$^{\text{th}}$ percentiles show that cases with much higher wind speeds are possible. The conditions for flow separation thus match the conditions for the formation of deep waves and warm-air intrusions over the crater described by Whiteman et al. (2018b).

The wind profiles in Fig. 5 show another distinct difference between flow intrusion and flow-separation regimes. For flow intrusions and quiescent conditions, near-surface wind speeds at NEAR and at RIM are very similar. Above approximately 15 m AGL, however, the wind speed at RIM is lower than at NEAR on average. This flow deceleration was already noticed in the case study of Whiteman et al. (2018a). Figure 3a shows the wind speeds at the first levels at NEAR and RIM for the night studied by Whiteman et al. (2018b), that is, at 3 and 5 m AGL, respectively. Close to the surface, the wind speed remains nearly constant between the upstream site and the crater rim, in agreement with the mean profiles in Fig. 5. In contrast, a mean flow acceleration occurs throughout the entire flow depth from NEAR to RIM during flow-separation cases. This flow acceleration can also be seen in the two case studies with a small and a large wake in Figs. 3d, g. In the latter, a flow acceleration of about 2–3 m s^{-1} occurs near the surface throughout most of the night. During the night of 16–17 October (Fig. 3d), flow separation is briefly interrupted around

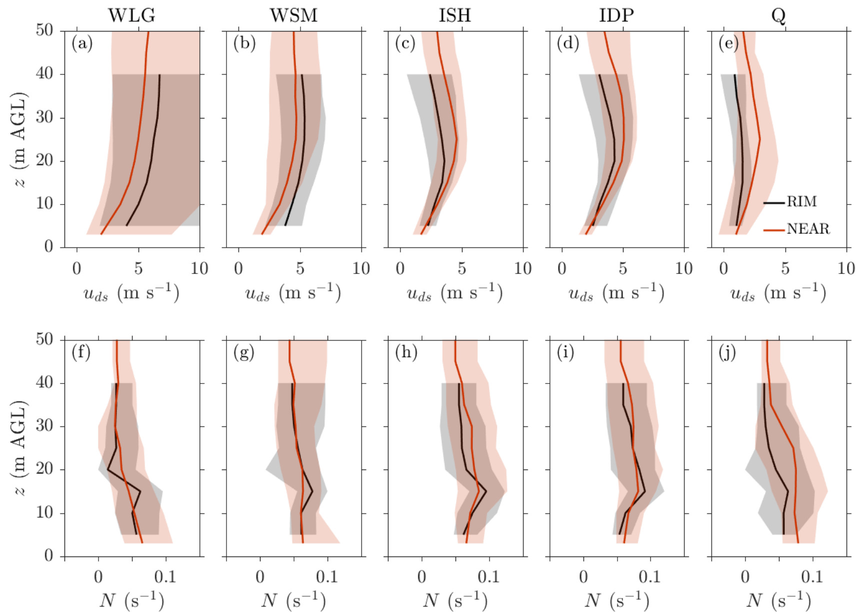

Fig. 5 Profiles of the (a–e) downslope wind component and (f–j) Brunt-Väisälä frequency at NEAR (red) and RIM (black) for the five different flow regimes. Profiles are median values and the shading indicates the 10$^{\text{th}}$ and 90$^{\text{th}}$ percentiles. The downslope wind component u_{ds} was calculated in the direction of the main topographic gradient of the upstream plain, that is, 215°.

0200 MST and then finally ends in the morning around 0430 MST. As mentioned before, these periods correspond to a decrease in wind speed at RIM, which, however, is not reflected in the upstream near-surface wind at NEAR, thus resulting in a reduced flow acceleration. Similarly, a brief drop in wind speed at RIM and thus in the flow acceleration upstream occurred during the night of 27–28 October (Fig. 3g) around 0100 MST together with a decrease in wind speed at FLR and with the development of a basin-floor inversion. As wind speeds remain low at both SSW2 and SSW4 during this time, flow separation is still occurring but only a smaller wake forms.

To gain further insight into the flow acceleration or deceleration between NEAR and RIM, the pressure gradient was examined between the two sites. For the determination of the horizontal pressure difference, the pressure at NEAR was extrapolated to the elevation of the pressure measurement at RIM using the hydrostatic equation. The pressure difference between RIM and NEAR is positive throughout the entire night of 26–27 October (Fig. 3c), that is, the pressure gradient opposes the southwesterly katabatic flow, consistent with the observed flow deceleration. During the nights of 16–17 October (Fig. 3f) and 27–28 October (Fig. 3i), on the other hand, the pressure difference is generally closer to zero or even negative. Times with a positive pressure difference match times with lower wind speeds at RIM and thus a break in flow

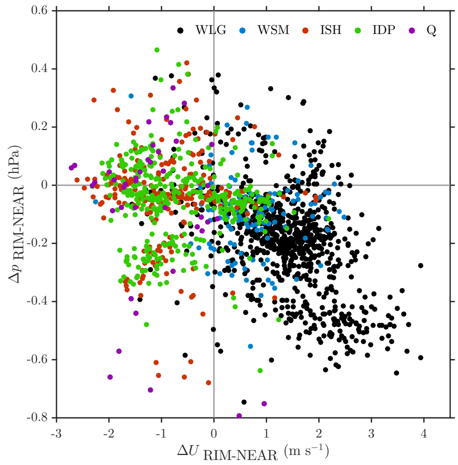

Fig. 6 Pressure difference between RIM and NEAR against mean-wind-speed difference between RIM and NEAR.

separation. Figure 6 shows the upstream change in the layer-averaged wind speed between NEAR and RIM together with the pressure difference between the two sites for all individual 5-min intervals. Flow separation, particularly large wakes affecting the entire southwest sidewall, occur mostly in the lower-right quadrant, where $\Delta p < 0$ and $\Delta U > 0$. This means that flow separation occurs when the pressure decreases towards the rim and the flow accelerates towards the rim. In contrast, flow intrusions occur generally with a flow deceleration. The pressure gradient, however, can point in either direction.

5 Conditions within the Wake Region

When flow separation occurs at the southwest crater rim, a wake forms over the inner southwest sidewall, whose size depends on the flow conditions. The wake is characterized by low wind speeds and sometimes a return circulation near the surface, that is, an upslope flow component (see Sect. 3). In this section, we will further analyze the conditions within the wake region, including its turbulence characteristics, stability, and pressure. Time series of potential temperature along the hobo line running up the SSW sidewall and time series of pressure deviations at several sites along the southwest sidewall are shown in Fig. 7 for the three case studies. The potential temperature time series from the south-southwest crater sidewall are overall very similar to the potential temperature time series from the northeast sidewall shown in Fig. 3, that is, they also show the development of the nocturnal crater inversion, which is disturbed during flow-separation events. In contrast to the northeast sidewall, however, the potential temperatures at the crater rim (indicated by the dark red lines in Fig. 7) are generally not the highest, but rather slightly lower than the potential temperatures in the upper part of the crater atmosphere. This slightly superadiabatic pseudo-vertical profile along the south-southwest sidewall has already been described by Whiteman et al. (2018a) for the intrusion case of the 26–27 October (Fig. 7a), who hypothesized that it is caused by turbulent mixing at the bottom of the shallow cold-air intrusion layer. During the night of 16–17 October the superadiabatic layer is even more pronounced, particularly during the first part of the night before the onset of flow separation (Fig. 7c). During the first wake formation around 0100 MST, the superadiabatic stratification is strongly reduced and the overall pseudo-vertical temperature gradient becomes close to neutral. Interestingly, the crater-floor temperature becomes even higher than the rim temperature when the crater inversion is destroyed by the formation of the wake—that is, a superadiabatic stratification develops in the lower part of the crater. This behaviour is particularly pronounced during the night of 27–28 October, when the crater-floor temperature becomes as high as the rim temperature and about 3°C higher than the temperatures along the SSW sidewall (Fig. 7e).

Median pseudo-vertical potential temperature profiles (Fig. 8a) along the southwest crater sidewall show that the superadiabatic stratification is also present on average during flow intrusions and during the formation of small wakes, with the wake cases on average colder than the intrusion cases. For completely quiescent cases, the temperature profile is close to the nocturnal temperature profile observed in other small basins under undisturbed conditions (Clements et al. 2003; Whiteman et al. 2004; Dorninger et al. 2011), with a continuously stably stratified layer to the top of the crater basin. Large wakes occur with strong winds at RIM, resulting in a well mixed crater atmosphere.

Pressure deviations on the southwest sidewall were calculated with respect to the NNE site on the relatively undisturbed northeast sidewall. To increase the comparability among the individual sites by removing the altitude effect, the mean pressure difference between each site and the NNE site between 2300 and 0600 MST was subtracted from the respective time series. With the exception of a weak diurnal trend, particularly at RIM, the pressure remains relatively constant throughout the night of 26–27 October, when no wakes form over the southwest sidewall (Fig. 7b). During the night of 16–17 October, the pressure along the southwest sidewall is affected by the formation, breakup, and subsequent reformation of the small wake (Fig. 7d). The pressure at RIM, SSW4, and SSW2 drops with the formation of a wake around midnight, increases to a positive peak during the short breakup of the wake around 0200 MST and then decreases again. It remains low until about 0400 MST at RIM and SSW4, although the pressure increases already somewhat earlier at SSW2. Even at SSW1 farther down the slope, a short drop in pressure is observed after 0200 MST. Interestingly, SSW3, which is located between SSW4 and SSW2, remains unaffected. Even during the night of 27–28 October, the brief weakening of the wake around 0100 MST, which is indicated by a stabilization of the crater atmosphere, leads to a brief increase in pressure at all sites (Fig. 7f). Average pressure perturbation profiles (Fig. 8b) suggest that during quiescent conditions and shallow intrusions the pressure is on average

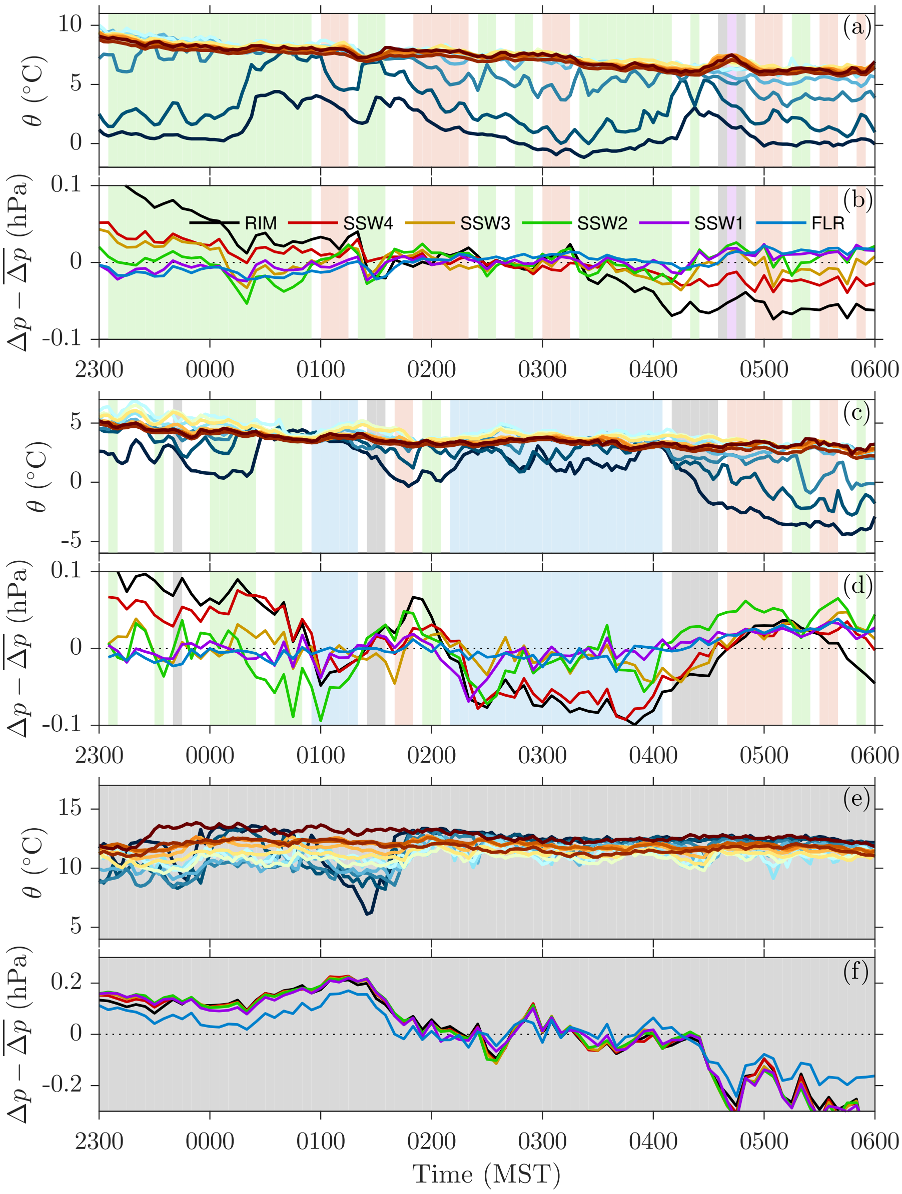

Fig. 7 Time series of (a,c,e) potential temperature at different sites running up the south-southwest hobo line from the crater floor (dark blue) to the rim (dark red) at 10–20 m height intervals and (b,d,f) pressure differences between sites along the southwest sidewall and a site on the opposite north-northeast sidewall on (a,b) 26–27, (c,d) 16–17, and (e,f) 27–28 Oct. The respective mean pressure difference $\overline{\Delta p}$ over the 7-h period between 2300 and 0600 MST was subtracted from each pressure time series for better comparability among the sites.

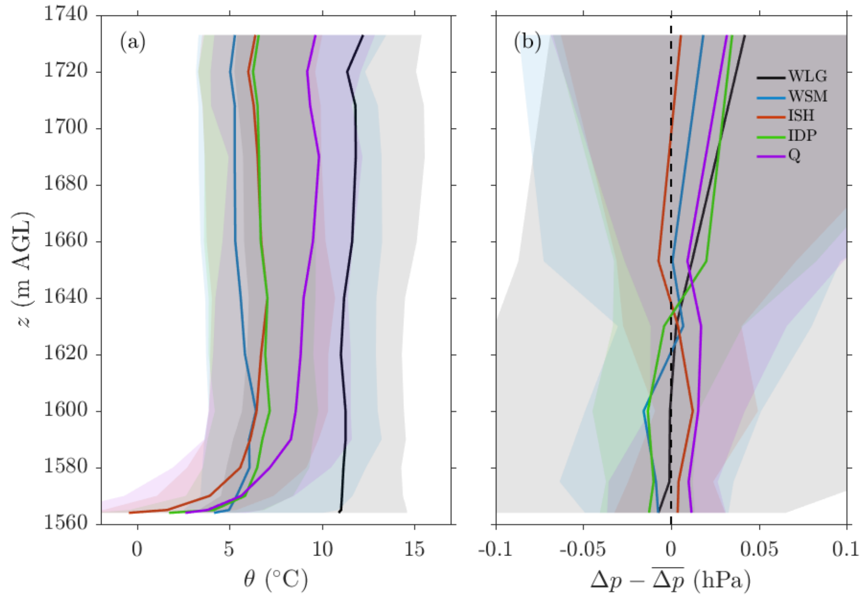

Fig. 8 Pseudo-vertical profiles of median (a) potential temperature and (b) pressure deviations along the south-southwest crater sidewall for the different flow regimes. Pressure deviations were calculated with respect to a reference site on the northeast sidewall and the mean over the period 2300–0600 MST was subtracted for better comparability among the sites. Shading indicates the 10^{th} and 90^{th} percentiles.

higher over the southwest sidewall than over the opposing northeast sidewall in the lower part of the crater, whereas during deeper intrusions and small wakes the pressure gradient reverses. During large wakes, the pressure distribution is relatively homogeneous. In the upper part of the crater, the pressure over the southwest sidewall is generally higher than over the northeast sidewall independent of the flow regime. It has to be kept in mind, however, that only one reference site, which is located in the lower part of the crater, exists on the northeast sidewall.

Turbulence characteristics in the wake region, such as turbulence kinetic energy (TKE), the velocity aspect ratio (Vickers and Mahrt 2006)

$$\mathrm{VAR} = \left(\frac{2\overline{w'^2}}{\overline{u'^2} + \overline{v'^2}} \right)^{1/2}, \tag{1}$$

momentum fluxes, and the vertical heat flux are shown for the three case studies in Fig. 9 and for the entire month in Fig. 10. In the absence of a wake over the southwest sidewall during the night of 26–27 October, TKE is generally low with the exception of SSW2 (Fig. 9a), which is located near the top of the basin-floor inversion and most of the time at the lower edge of cold-air inflow (Fig. 3a). TKE at SSW2 is dominated by contributions from the horizontal velocity variances $\overline{u'^2}$ and $\overline{v'^2}$. While TKE is generally weak at the other sites, VAR is closer to 1 at RIM and to a lesser degree at SSW4, meaning that $\overline{w'^2}$ has a similar magnitude as $\overline{u'^2}$ and $\overline{v'^2}$ and turbulence is closer to isotropic. During the night of 16–17 October, TKE at SSW4 reaches values similar to SSW2 (Fig. 9e). This increase in TKE compared to the night of 26–27 October is due to an increase in the variances of all three velocity components, but particularly after 0200 MST, $\overline{u'^2}$ and $\overline{v'^2}$ increase more strongly than $\overline{w'^2}$, leading to a decrease in VAR. TKE increases strongly at the basin floor and at the crater rim when a large wake forms during the night of 27–28 October, with comparatively low values along the southwest sidewall (Fig. 9i). VAR also remains relatively low during this night (Fig. 9j).

The generally low values of TKE at RIM and FLR, with the exception of large wakes when particularly $\overline{u'^2} + \overline{v'^2}$ increases significantly, can be observed throughout the entire month (Figs. 10a, d). On the other hand, large wakes are generally characterized by low TKE at both SSW2 and SSW4 (Figs. 10b, c). For small wakes, the increase in TKE at SSW2 observed during the night of 16–17 October is also seen throughout the month (Fig. 10c). At SSW4, however, the small wakes show relatively large scatter of both $\overline{w'^2}$ and $\overline{u'^2} + \overline{v'^2}$ (Fig 10b). For intrusions, the analysis of the entire month shows a slightly different picture than just the night of 26–27 October. It can be clearly seen that at SSW4, TKE is generally higher during intrusions than during wake events, with an increase in both $\overline{w'^2}$ and $\overline{u'^2} + \overline{v'^2}$. Similarly, larger TKE values occur at SSW2 during deep intrusion events, when the cold-air intrusions actually reach the site, with relatively large scatter during the less deep intrusion events (Fig 10c). In contrast to SSW4, however, the increase in TKE at SSW2 is generally due to in increase in $\overline{u'^2} + \overline{v'^2}$, while $\overline{w'^2}$ remains low.

The horizontal momentum fluxes are also influenced by the formation of a wake over the southwest sidewall. The streamwise momentum flux $\overline{u'w'}$ is generally positive at SSW4 and SSW2 during both the night of 26–27 October (intrusions; Fig. 9c) and the night of 16–17 October (small wake; Fig. 9g), with negligible values at RIM and at FLR. As a small wake forms during the night of 16–17 October, $\overline{u'w'}$ increases at SSW2 compared to the intrusion night of 26–27 October, with a weak minimum between 0100 and 0200 MST together with the brief breakup of the wake. The lateral momentum flux $\overline{v'w'}$ increases as well (not shown), but remains small compared to the streamwise component. Based on the wind speed, it had been established that small wakes do not affect SSW2 but only SSW4 farther up the slope. The close correlation between the momentum flux at SSW2 and the timing of the wake, however, suggests that SSW2 is affected, even though the wake does not extend this far down the sidewall. This may be related to another phenomenon, that is, the formation of gravity waves and associated warm-air intrusions (Whiteman et al. 2018b), which form under similar conditions as small wakes. This will be further discussed in Sect. 6.

The increase in momentum flux at SSW2 for small wakes can also be seen throughout the month, but with relatively large scatter (Fig. 10g). Increased values in $\overline{u'w'}$ result also from deep intrusions reaching the lower sidewall. At SSW4, positive values of momentum flux are observed during all intrusions and

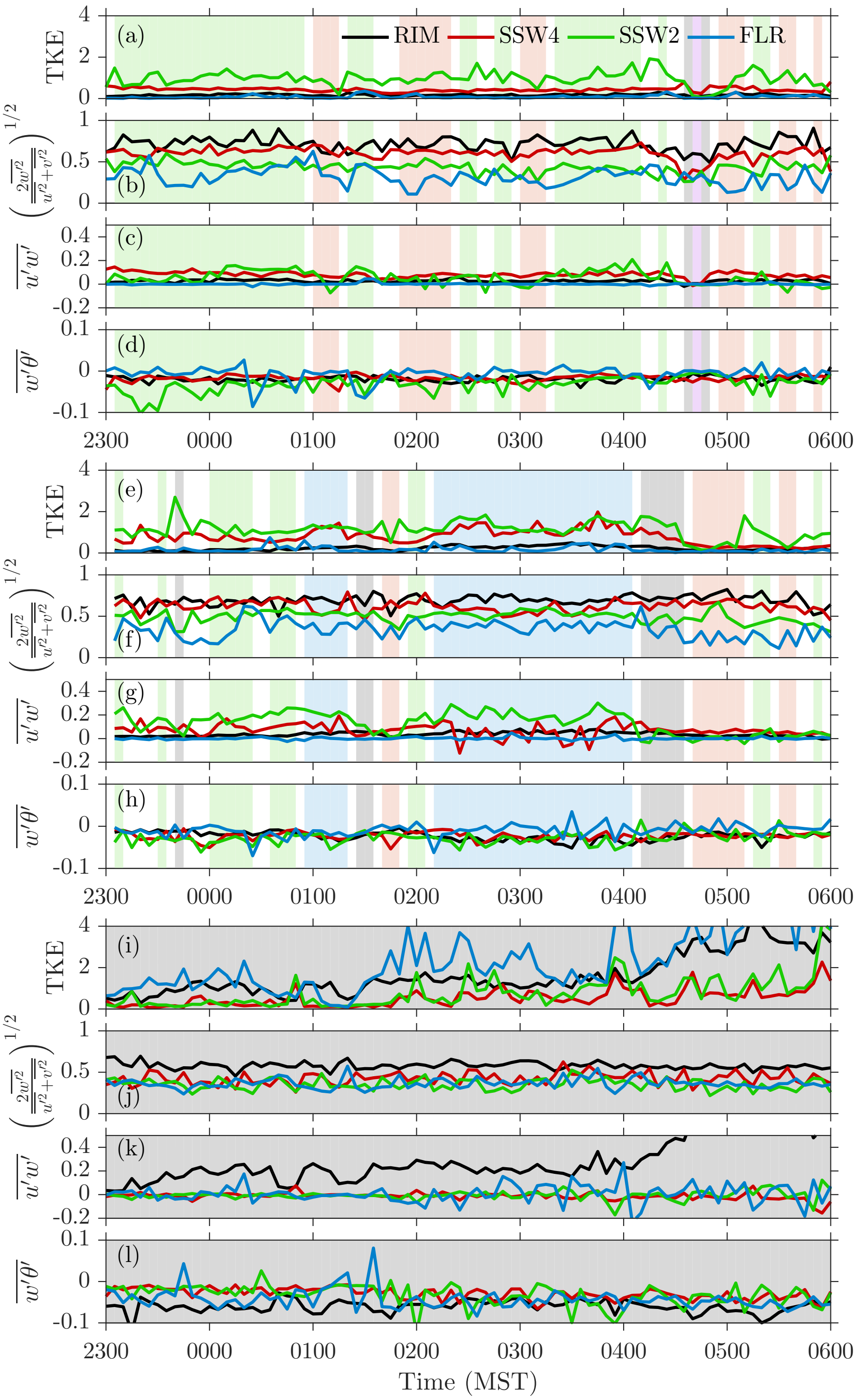

Fig. 9 Time series of (a,e,i) TKE, (b,f,j) the velocity aspect ratio, (c,g,k) the streamwise momentum flux, and (d,h,l) the vertical heat flux on (a–d) 26–27, (e–h) 16–17, and (i–l) 27–28 Oct.

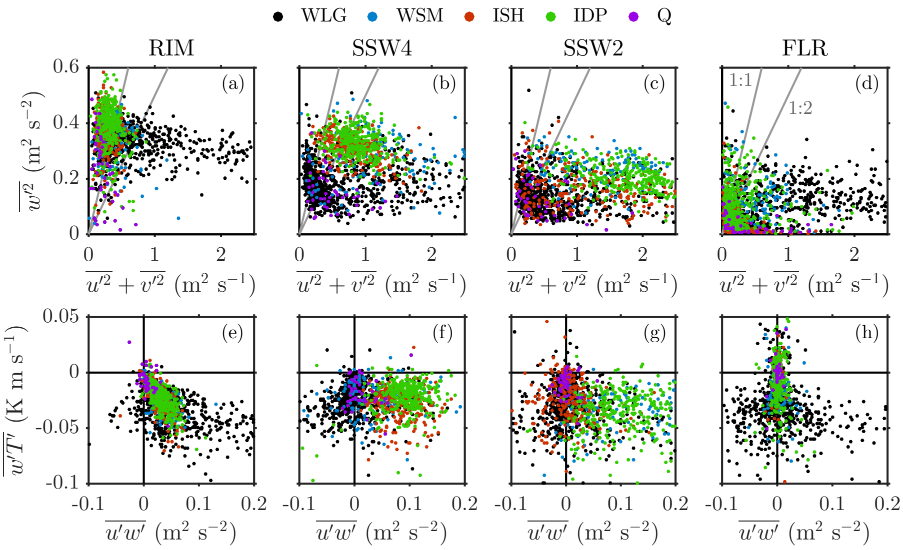

Fig. 10 (a–d) Contributions of $\overline{u'^2} + \overline{v'^2}$ and $\overline{w'^2}$ to TKE and (e–h) vertical heat flux and streamwise momentum flux at (a,e) RIM, (b,f) SSW4, (c,g) SSW2, and (d,h) FLR.

close to zero or negative values during wakes (Fig. 10f). The generally positive values during intrusions suggest that the cold-air intrusions are extremely shallow, with the highest wind speeds located below the measurement height of 3 m AGL, resulting in an upward momentum transport.

During large wakes (e.g., 27–28 October, Fig. 9h) the momentum fluxes at RIM and sometimes at FLR can increase in magnitude, with relatively low values at the other sites (Fig. 10e–h). However, while the momentum flux at RIM remains positive, negative values are equally possible at FLR.

In the vertical heat flux, there is little difference between intrusions and wakes. It is overall negative at all sites, consistent with stable conditions, with values close to zero during intrusions and small wakes (Figs. 9b, d and Figs. 10e–h). Some small positive values are possible at FLR (Fig. 10b). The magnitude of the heat flux is generally independent of the flow regime (Figs. 10e–h). During the night of 27–28 October, however, when a large wake forms, the heat flux increases in magnitude at all sites despite the almost neutral stratification during this time (Fig. 9l).

Scintillometer measurements were made across the southwest part of the crater to observe turbulence in the immediate lee of the rim (Fig. 1), where the flow separates from the surface. A time series of the refractive index structure parameter C_n^2 is shown in Fig. 11 for the night of 16–17 October. C_n^2 is a measure for the spatial variability of the refractive index of air and thus for turbulence intensity. During this night, C_n^2 increased around 0200 MST together with the onset of flow separation, indicating increased turbulence near the top of the crater compared to time periods with flow intrusions. A similar, although much weaker, increase was also observed during the shorter

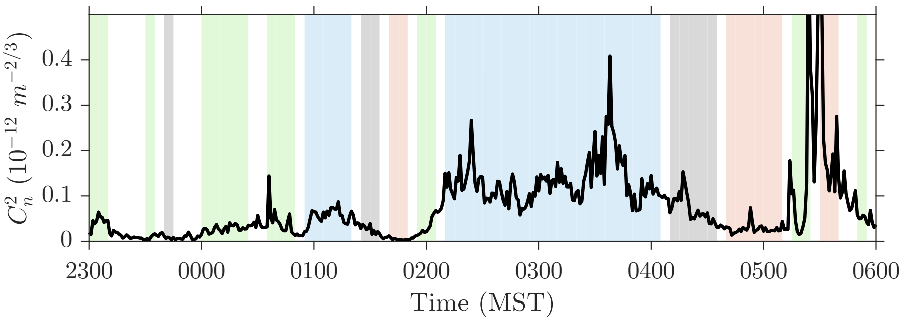

Fig. 11 Time series of the refractive index structure parameter on 16–17 Oct. Background color shading as in Fig. 3.

period of flow separation around 0100 MST. A statistical comparison of C_n^2 for the five different flow categories for the whole month revealed, however, similar median values for small wakes and the two intrusion categories and even a lower 75 percentile (not shown). Large wakes, on the other hand, have statistically slightly higher C_n^2 values. It is conceivable that the small wakes were oftentimes too shallow to be captured by the scintillometer path. The available measurements during METCRAX II, however, did not allow for a determination of the actual slope-normal wake depth.

6 Summary and Discussion

Observations have been presented from the METCRAX II field campaign in the approximately 170-m deep and 1.2-km wide Meteor Crater in Arizona that show that wakes can form over the inner southwest crater sidewall. The wakes are characterized by low wind there, but are speeds coincident with relatively high wind speeds at the crater rim and at the crater floor. The Meteor Crater is located on an extensive plain that slopes slightly upwards to the southwest, so that a southwesterly katabatic flow forms in connection with a surface-based inversion during quiescent and undisturbed nights. As the southwesterly katabatic wind flows over the approximately 30–50-m high crater rim, the flow can either run down the southwest sidewall because the air is colder than the ambient crater atmosphere or it can separate from the surface leading to the formation of a wake over the inner sidewall.

The analysis has focused on nighttime data from the one-month long measurement campaign. The data were classified into five different regimes based on wind speed observations at the southwest crater rim and at two sites on the southwest inner sidewall: flow separation with the formation of either (i) large wakes that affect the entire southwest sidewall (WLG) or (ii) small wakes that affect only the upper part of the southwest sidewall (WSM), (iii) deep and (iv) shallow cold-air intrusions when no wake forms but part of the upstream drainage flow runs down the sidewall until it reaches its level of neutral buoyancy (IDP and ISH), and finally, (v) quiescent conditions (Q). Schematic

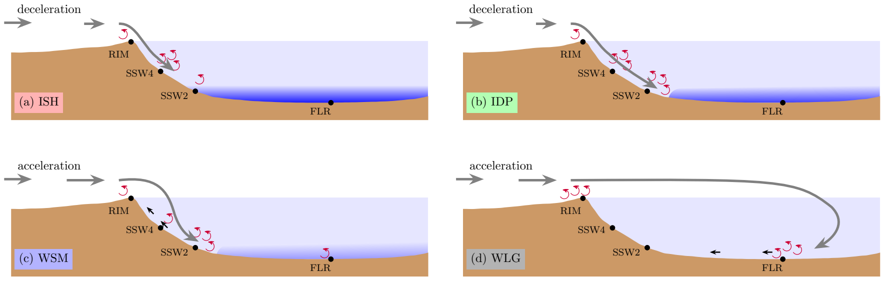

Fig. 12 Schematic diagrams of (a) shallow intrusions, (b) deep intrusions, (c) small wakes, and (d) large wakes. Small black arrows show potential recirculation zones and small red eddies indicate turbulence, with a larger number of eddies indicating higher TKE.

diagrams of the two wake regimes and the two intrusion regimes in Fig. 12 summarize the findings from the analysis of the upstream conditions leading to flow separation and the mean and turbulence conditions in the crater, particularly within the wake region. The classification scheme is of course strongly site dependent. For example, it is easily conceivable that very small wakes form over the upper part of the crater sidewall that do not even extend to SSW4 and are thus classified as intrusion regimes. Similarly, the classification into deep versus shallow intrusions and large versus small wakes is based on wind-speed observations at SSW2, a site approximately 50 m above the crater floor. Observations at a lower or higher site may lead to different classifications. A thorough analysis of a cold-air intrusion dominated night is presented by Whiteman et al. (2018a). As also shown in the work by Whiteman et al. (2018a), cold-air intrusions (Figs. 12a, b) form when the upstream katabatic flow is shallow according to the classification by Stiperski et al. (2018) and the flow decelerates towards the crater. As the lower part of the drainage flow is colder than the crater atmosphere, the cold air can run down the sidewall until it reaches its level of neutral buoyancy. The location of the level of neutral buoyancy determines whether shallow (Fig. 12a) or deep (Fig. 12b) intrusions form, that is, whether the intrusion reaches to the measurement site in the lower part of the sidewall. The crater atmosphere is typically strongly stratified in the lowest layer during intrusions, but relatively strong turbulence is observed in the vicinity of the intrusion flow. While the lower part of the southwest sidewall is thus typically characterized by quiescent conditions for shallow intrusions, wind speed and turbulence increase and stability decreases for deep intrusions.

For the analysis, a fifth, quiescent regime was defined, which was used to filter out data with overall low wind speeds, both at the crater rim and along the southwest crater sidewall. Based on our classification method, whose main criterion is the wind speed on the sidewall, these data would have otherwise not been distinguishable from the flow separation regimes, which, however, form only under higher wind speeds. The general conditions both upstream (e.g., wind speed and profiles) and in the crater (e.g., stability) during these quiescent periods are very similar to intrusions. This category is thus not a separate physical regime, but rather consists of intrusions under very weak wind conditions.

The occurrence of flow separation and subsequent wake formation generally matches the criterion for bluff-body flow separation by Baines (1995), that is, that the leeside half-length of the obstacle is smaller than the half wavelength of the internal waves excited by the obstacle. Estimating the half-length of the crater sidewall, the resulting criterion becomes $N/U < 0.02\ \mathrm{m}^{-1}$ for the Meteor Crater, that is, flow separation is facilitated by lower stability and higher wind speeds. Observations show that the wind speed at the crater rim plays a crucial role, with flow separation becoming the dominant regime for layer-averaged wind speeds larger than 5 m s^{-1}. The upstream wind profile during conditions leading to flow separation is typically characterized by a deep katabatic flow according to the classification by Stiperski et al. (2018) and the flow accelerates towards the crater, with the horizontal pressure gradient just upwind of the crater rim opposing the direction of the katabatic flow (Figs. 12c, d).

Flow separation leading to the formation of small wakes is summarized in Fig. 12c. The slope-normal extent of the wake is probably exaggerated in the schematic diagram. Lidar scans were performed from a site slightly below SSW2, but the small wakes seem to be too small to be seen by the lidar scans. For small wakes, the upper part of the sidewall is characterized by low wind speeds and low turbulence compared to the lower part of the sidewall. While the wake does not extend to the lower part of the sidewall, conditions at the lower sidewall and also at the crater floor still show some correlation with the formation of the wake, for example, increased wind speeds and momentum fluxes and reduced stability. The conditions leading to flow separation and the formation of small wakes are, however, similar to the conditions leading to the formation of deep gravity waves over the crater and the associated downward transport of warm air into the crater from above (Whiteman et al. 2018b). The night analyzed by Whiteman et al. (2018b) (IOP4; 19–20 October) is overall very similar to the night of 16–17 October, that is, our case study for small-wake formation. This suggests that small wakes may occur together with a deep wave downstream, which causes the increased wind speeds at SSW2 and the increased mixing and destabilization in the lower part of the crater. An open question is whether the reduced stability in the crater as a result of the gravity waves facilitates flow separation at the rim. Whiteman et al. (2018b) also identified a transitional period when the flow over the crater rim bifurcates leading to a quiescent, wake-like flow region between the two bifurcating flow layers over the southwest part of the crater, which they called a cavity. This cavity, however, is not identical with the wake region identified here, which forms below the intruding flow (Fig. 12c), whereas the cavity is located above the intruding branch of the flow (see their Fig. 11).

With very high wind speeds upstream (more than about 7 m s^{-1}) only large wakes form, whereas for lower wind speeds either small or large wakes can form. A schematic diagram of this regime is presented in Fig. 12d. No direct observations of the large, crater-size eddy indicated in Fig. 12d are available. Observations from the crater floor, however, show a return circulation that opposes the southwesterly flow above the crater and pseudo-vertical temperature profiles along the crater sidewalls indicate a well-mixed crater atmosphere. Similar conditions that are representative of our large wake cases were simulated by Katurji et al. (2013), who performed idealized simulations of flow over a basin with a size similar to the Meteor Crater, with high wind speeds of 10 m s^{-1} and neutral stratification.

The observation of flow separation at the crater rim has yielded another detail in the understanding of the complex nocturnal flow at the Meteor Crater and the different flow regimes resulting from the interaction of the southwesterly katabatic flow with the crater topography. While the available observations have not allowed a direct visualization or a determination of the exact size of the eddy or wake resulting from flow separation, the data have provided a detailed description of the flow characteristics within the wake and downstream of the wake and allowed the analysis of the conditions leading to flow separation at the crater rim.

Acknowledgements This research was supported by the National Science Foundations Physical and Dynamic Meteorology Division through Grant AGS-1160730. The contributions from KIT was funded by the International Bureau of BMBF under Grant 01 DM 13002. We thank the many METCRAX II collaborators and volunteers helping in the field, the property owners for field access, and the colleagues who provided additional equipment, who are all listed as either coauthors or in the acknowledgment section of Lehner et al. (2016b).

References

Adler B, Whiteman CD, Hoch SW, Lehner M, Kalthoff N (2012) Warm-air intrusions in Arizona's Meteor Crater. J Appl Meteorol Climat 51:1010–1025, DOI 10.1175/JAMC-D-11-0158.1

Ambaum MHP, Marshall DP (2005) The effects of stratification on flow separation. J Atmos Sci 62:2618–2625, DOI 10.1175/JAS3485.1

Arya SPS, Capuano ME, Fagen LC (1987) Some fluid modeling studies of flow and dispersion over two-dimensional low hills 21:753–764, DOI 10.1016/0004-6981(87)90071-0

Baines PG (1995) Topographic Effects in Stratified Flow. Cambridge University Press

Baines PG, Hoinka KP (1985) Stratified flow over two-dimensional topography in fluid of infinite depth: A laboratory simulation. J Atmos Sci 42:1614–1630, DOI 10.1175/1520-0469(1985)042⟨1614:SFOTDT⟩2.0.CO;2

Batchelor GK (1967) An Introduction to Fluid Dynamics. Cambridge University Press, DOI 10.1017/CBO9780511800955

Belcher SE, Hunt JCR (1998) Turbulent flow over hills and waves. Ann Rev Fluid Mech 30:507–538, DOI 10.1146/annurev.fluid.30.1.507

Clements CB, Whiteman CD, Horel JD (2003) Cold-air-pool structure and evolution in a mountain basin: Peter Sinks, Utah. J Appl Meteorol 42:752–768, DOI 10.1175/1520-0450(2003)042⟨0752:CSAEIA⟩2.0.CO;2

Dorninger M, Whiteman CD, Bica B, Eisenbach S, Pospichal B, Steinacker R (2011) Meteorological events affecting cold-air pools in a small basin. J Appl Meteorol Climat 50:2223–2234, DOI 10.1175/2011JAMC2681.1

Doyle JD, Durran DR (2002) The dynamics of mountain-wave-induced rotors. J Atmos Sci 59:186–201, DOI 10.1175/1520-0469(2002)059⟨0186:TDOMWI⟩2.0.CO;2

Doyle JD, Durran DR (2007) Rotor and subrotor dynamics in the lee of three-dimensional terrain. J Atmos Sci 64:4202–4221, DOI 10.1175/2007JAS2352.1

French JR, Haimov SJ, Oolman LD, Grubišić V, Serafin S, Strauss L (2015) Wave-induced boundary layer separation in the lee of the Medicine Bow Mountains. part I: Observations. J Atmos Sci 72:4845–4863, DOI 10.1175/JAS-D-14-0376.1

Gerber F, Lehning M, Hoch SW, Mott R (2017) A close-ridge small-scale atmospheric flow field and its influence on snow accumulation. J Geophys Res Atm 122:7737–7754, DOI 10.1002/2016JD026258

Grubišić V, Doyle JD (2006) Terrain-induced Rotor Experiment. In: 12th Conference on Mountain Meteorology, American Meteorological Society, Santa Fe, New Mexico, USA

Haiden T, Whiteman CD, Hoch SW, Lehner M (2011) A mass flux model of nocturnal cold-air intrusions into a closed basin. J Appl Meteorol Climat 50:933–943, DOI 10.1175/2010JAMC2540.1

Hertenstein RF, Kuettner JP (2005) Rotor types associated with steep lee topography: influence of the wind profile. Tellus 57A:117–135, DOI 10.1111/j.1600-0870.2005.00099.x

Holden JJ, Derbyshire SH, Belcher SE (2000) Tethered balloon observations of the nocturnal stable boundary layer in a valley. Boundary-Layer Meteorol 97:1–24, DOI 10.1023/A:1002628924673

Jackson PL, Mayr G, Vosper S (2012) Dynamically-driven winds. In: Chow FK, DeWekker SFJ, Snyder B (eds) Mountain Weather Research and Forecasting, Springer, Berlin, chap 3, 121–218

Katurji M, Zhong S, Kiefer M, Zawar-Reza P (2013) Numerical simulations of turbulent flow within and in the wake of a small basin. J Geophys Res 118:6052–6063, DOI 10.1002/jgrd.50519

Kim JJ, Baik JJ, Chun HY (2001) Two-dimensional numerical modeling of flow and dispersion in the presence of hill and buildings. J Wind Eng Ind Aerodyn 89:947–966, DOI 10.1016/S0167-6105(01)00092-7

Lehner M, Rotunno R, Whiteman CD (2016a) Flow regimes over a basin induced by upstream katabatic flows—an idealized modeling study. J Atmos Sci 73:3821–3842, DOI 10.1175/JAS-D-16-0114.1

Lehner M, Whiteman CD, Hoch SW, Crosman ET, Jeglum ME, Cherukuru NW, Calhoun R, Adler B, Kalthoff N, Rotunno R, Horst TW, Semmer S, Brown WOJ, Oncley SP, Vogt R, Grudzielanek AM, Cermak J, Fonteyne NJ, Bernhofer C, Pitacco A, Klein P (2016b) The METCRAX II field experiment—a study of downslope windstorm-type flows in Arizona's Meteor Crater. Bull Amer Meteorol Soc 97:217–235, DOI 10.1175/BAMS-D-14-00238.1

Mason PJ (1987) Diurnal variations in flow over a succession of ridges and valleys. Q J R Meteorol Soc 113:1117–1140, DOI 10.1002/qj.49711347804

Menke R, Vasiljević N, Mann J, Lundquist JK (2018) Characterisation of recirculation zones in complex terrain using multi-lidar measurements. In: AMS 18th Conference on Mountain Meteorology

Patton EG, Katul GG (2009) Turbulent pressure and velocity perturbations induced by gentle hills covered with sparse and dense canopies. Boundary-Layer Meteorol 133:189–217, DOI 10.1007/s10546-009-9427-x

Poggi D, Katul GG (2007) Turbulent flows on forested hilly terrain: the recirculation region. Q J R Meteorol Soc 133:1027–1039, DOI 10.1002/qj.73

Rotunno R, Lehner M (2016) Two-layer stratified flow past a valley. J Atmos Sci 73:4065–4076, DOI 10.1175/JAS-D-16-0132.1

Smolarkiewicz PK, Rotunno R (1989) Low Froude number flow past three-dimensional obstacles. part I: Baroclinically generated lee vortices. J Atmos Sci 46:1154–1164, DOI 10.1175/1520-0469(1989)046⟨1154:LFNFPT⟩2.0.CO;2

Stiperski I, Whiteman CD, Holtslag AAM, Lehner M, Hoch SW (2018) On the turbulence structure, dominant scales and scaling of deep katabatic flows on a shallow mesoscale slope. Q J R Meteorol Soc in preparation

Strauss L, Serafin S, Haimov S, Grubišić V (2015) Turbulence in breaking mountain waves and atmospheric rotors estimated from airborne in situ and Doppler radar measurements. Q J R Meteorol Soc 141:3207–3225, DOI 10.1002/qj.2604

Strauss L, Serafin S, Grubišić V (2016) Atmospheric rotors and severe turbulence in a long deep valley. J Atmos Sci 73:1481–1506, DOI 10.1175/JAS-D-15-0192.1

Vickers D, Mahrt L (2006) A solution for flux contamination by mesoscale motions with very weak turbulence. Boundary-Layer Meteorol 118:431–447, DOI 10.1007/s10546-005-9003-y

Voigt M, Wirth V (2013) Mechanisms of banner cloud formation. J Atmos Sci 70:3631–3640, DOI 10.1175/JAS-D-12-0353.1

Vosper SB (2004) Inversion effects on mountain lee waves. Q J R Meteorol Soc 130:1723–1748, DOI 10.1256/qj.03.63

Whiteman CD, Eisenbach S, Pospichal B, Steinacker R (2004) Comparison of vertical soundings and sidewall air temperature measurements in a small Alpine basin. J Appl Meteorol 43:1635–1647, DOI 10.1175/JAM2168.1

Whiteman CD, Muschinski A, Zhong S, Fritts D, Hoch SW, Hahnenberger M, Yao W, Hohreiter V, Behn M, Cheon Y, Clements CB, Horst TW, Brown WOJ, Oncley SP (2008) METCRAX 2006—Meteorological experiments in Arizona's Meteor Crater. Bull Amer Meteorol Soc 89:1665–1680, DOI 10.1175/2008BAMS2574.1

Whiteman CD, Hoch SW, Lehner M, Haiden T (2010) Nocturnal cold air intrusions into a closed basin: Observational evidence and conceptual model. J Appl Meteorol Climat 49:1894–1905, DOI 10.1175/2010JAMC2470.1

Whiteman CD, Lehner M, Hoch SW, Adler B, Kalthoff N, Haiden T (2018a) Katabatically driven cold air intrusions into a basin atmosphere. J Appl Meteorol Climat 57:435–455, DOI 10.1175/JAMC-D-17-0131.1

Whiteman CD, Lehner M, Hoch SW, Adler B, Kalthoff N, Vogt R, Feigenwinter I, , Haiden T, Hills MOG (2018b) The nocturnal evolution of atmospheric structure in a basin as a larger-scale katabatic flow is lifted over its rim. J Appl Meteorol Climat 57:969–989, DOI 10.1175/JAMC-D-17-0156.1

Wilczak JM, Oncley SP, Stage SA (2001) Sonic anemometer tilt correction algorithms. Boundary-Layer Meteorol 99:127–150

Wirth V, Kristen M, Leschner M, Reuder J, Schween JH (2012) Banner clouds observed at Mount Zugspitze. Atmos Chem Phys 12:3611–3625, DOI 10.5194/acp-12-3611-2012

Wood N (1995) The onset of separation in neutral, turbulent flow over hills. Boundary-Layer Meteorol 76:137–164, DOI 10.1007/BF00710894